Image-based calibration of rolling resistance in discrete element models of sand

Rorato R., Arroyo M., Gens A., Andò E., Viggiani, G.

Riccardo Rorato, Dr.
Universitat Politécnica de Catalunya (UPC), Barcelona (Spain) - Department of Civil and Environmental Engineering.
riccardo.rorato@upc.edu
ORCID ID: 0000-0002-4189-3058
UPC - Barcelonatech
Moduli D2 Campus Nord UPC – Office 212
C Jordi Girona 1-3
Barcelona 08034

Marcos Arroyo Alvarez de Toledo, Prof.
Universitat Politécnica de Catalunya (UPC), Barcelona (Spain) - Department of Civil and Environmental Engineering
marcos.arroyo@upc.edu
ORCID ID: 0000-0001-9384-9107

Edward Carlo Giorgio Andò, Prof.
Univ. Grenoble Alpes, CNRS, Grenoble INP, 3SR, F-38000 Grenoble (France)
edward.ando@3sr-grenoble.fr
ORCID ID: 0000-0001-5509-5287

Antonio Gens Solé, Prof.
Universitat Politécnica de Catalunya (UPC), Barcelona (Spain) - Department of Civil and Environmental Engineering
antonio.gens@upc.edu
ORCID ID: 0000-0001-7588-7054

Gioacchino Viggiani, Prof.
Univ. Grenoble Alpes, CNRS, Grenoble INP, 3SR, F-38000 Grenoble (France)
cino.viggiani@3sr-grenoble.fr
ORCID ID: 0000-0002-2609-6077

Abstract

Models that introduce rolling resistance at the contact are widely employed in simulations using the discrete element method (DEM) to indirectly represent particle shape effects. This approach offers substantial computational benefits at the price of increased calibration complexity. This work proposes a method to simplify calibration of rolling resistance. The key element is an empirical relation between a contact parameter (*rolling friction*) and a 3D grain shape descriptor (*true sphericity)*. Values of true sphericity can be obtained by image analysis of the grains, either directly by 3D acquisition or by correlation with simpler-to-obtain 2D shape measures. Evaluation of rolling friction is thus made independent from that of other model parameters. As an extra benefit, the variability of grain shape in natural sands can be directly mapped into the discrete model. A mapping between rolling friction and true sphericity is calibrated using specimen-scale and grain scale results from two triaxial compression tests on Hostun sand and Caicos ooids. The mapping is validated using different triaxial tests from the same sands and from other reference sands (Ottawa, Ticino). In the case of Ticino grain-shape acquisition is made in 2D, using an ordinary table scanner. The results obtained support this direct calibration procedure.

Keywords: Discrete Element Method; Rolling Resistance; Particle Shape; X-rays micro tomography; Triaxial Test; Shear Resistance.

1 Introduction

Powered by increased computational performance, the discrete element method (DEM) has gained much relevance in geomechanics since originally proposed by Cundall & Strack (1979). DEM models at specimen scale are now a basic tool of research to study and illuminate many features of soil mechanics observed in the laboratory (Ciantia et al. 2019a; Li et al. 2018; Hosn et

2

al. 2018). There is also a growing trend to use DEM models to analyse large scale problems of direct engineering relevance (Zhang et al 2019; Zhang & Evans, 2019; Butlanska et al. 2018; Kawano et al. 2018). As in other numerical modelling approaches, there is always an underlying conflict between model resolution and computational efficiency. This tension is particularly vivid in the consideration of particle shapes in DEM.

The most widely used shape in 3D DEM is the sphere (as is the disk in 2D DEM). The reason is pragmatic: spheres allow straightforward and computationally efficient contact detection, which is a large part of the computational cost of every step. Unfortunately soil particles are not generally spherical but have instead very varied shapes. In coarse soils, research has clearly identified large particle shape effects for several important properties such as extreme void ratios (Cho et al. 2006), critical state friction (Yang and Luo 2015) or dilatancy and peak friction (Xiao et al. 2019). Particle shape also affects responses of major engineering significance, like liquefaction resistance (Vaid et al. 1985) or cone tip resistance (Liu & Lehane 2013).

Direct experimental evidence for the role of shape in soils was reinforced by DEM models in which grain shape was directly controlled. For instance, just switching from disks to ellipses (Rothemburg & Bathurst, 1992) or from spheres to ellipsoids (Lin & Ng, 1998) raised numerical shear strength and dilatancy values to within the range observed in soils.

Ellipses and ellipsoids are still far from the shapes observed in most soil particles. Several techniques have been developed to incorporate more realism into element shapes: they use clumps or aggregates of spheres (Matsushima 2002, Lu and McDowell 2007, Katagiri et al. 2010); polyhedrons (Zhao et al. 2006; Boon et al. 2012); superquadrics (Williams & Pentland, 1992; Zhao et al. 2018) or level sets (Jerves et al. 2016, Kawamoto et al. 2018). Increased morphological realism has advantages and disadvantages. One advantage is that it may be thus possible to represent the

84 non-negligible variability in shape that is observed in granular soils. A significant disadvantage

85 is added computational cost. Indeed, for the same problem dimensions, orders of magnitude in-

86 creases in computational time with respect to sphere-based models are typically reported (Lu et

87 al. 2015; Irazabal et al. 2017).

88

89 The micromechanics underlying the effect of element shape on shear strength was clarified by

90 Bardet (1994), who noted that disks showed a high concentration of rotations in shear bands and

91 that, if rotation was blocked, realistic values of friction and dilatancy ensued. Based on this and

92 similar observations, several researchers (Sakaguchi et al. 1993, Iwashita & Oda 1998, Jiang et al.

93 2005; Mohamed & Gutierrez, 2010) proposed the introduction of a resisting moment (*i.e., rolling*

94 *resistance*) at particle contacts (see Figure 1). The moment applied is typically dependent on rela-

95 tive particle rotation, opposing it through an elasto-plastic mechanism analogous to that acting

96 for contact forces. Sometimes a viscous component is also added to the contact formulation (see

97 Ai et al. 2011, for a review).
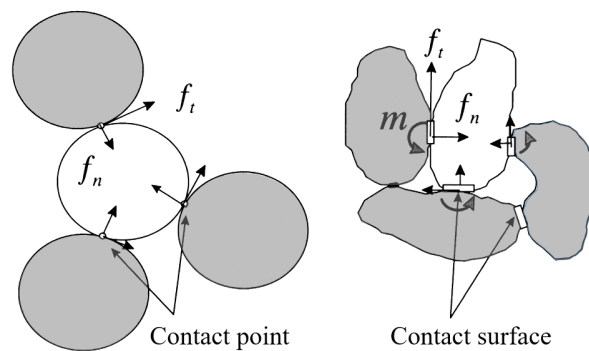
98

99 *Figure 1: Origin of rolling resistance at contact (Iwashita and Oda 1998)*

100 Several DEM studies (Zhou et al. 2013, Wensrich et al. 2014) have compared the results obtained

101 using aggregates of particles (*i.e.*, clumps) or adding rotational constrains, showing that both ap-

102 proaches result in very similar behaviour, at least for the quasi-static conditions relevant in most

103 soil mechanics problems. The main advantage of the rolling resistance model is that contact de-

104 tection remains efficient; the calibration of contact properties is, however, far from trivial.

105   The majority of the previous studies (Iwashita and Oda 1998, 2000, Jiang et al. 2005, Belheine et

106   al. 2009, Zhou et al. 2013) calibrate rolling resistance through an empirical macroscopic approach.

107   Specimen-scale responses of "identical" numerical and experimental test are matched by trial-

108   and-error. The process is difficult because the effects of rolling resistance in macro-response are

109   coupled with those of other parameters (the coefficient of sliding friction in particular), and mul-

110   tiple solutions are possible to match key experimental results, such as dilatancy or peak mobilised

111   friction (Estrada et al. 2008, Wensrich and Katterfeld 2012, Cheng et al. 2017). Calibration can thus

112   become a very time consuming and somewhat subjective process. Alternatives based on

113   statistically driven semi-automated calibration have been proposed, (Cheng et al. 2018) but they

114   appear computationally intensive.

115

116   Some researchers (Calvetti et al. 2003, Arroyo et al. 2011, Ciantia et al. 2015) have simplified

117   radically the calibration process by directly assuming very large values of moment resistance and

118   stiffness, so as to inhibit relative rotation at the contact. This assumption does not limit the ability

119   of the resulting discrete model to match and predict large-scale soil responses, but it does lack

120   some subtlety.

121

122   A different approach to simplify the calibration problem would be to give some specific physical

123   base to rolling resistance. Little work has been done to explore this possibility. Wensrich & Kat-

124   terfeld (2012) proposed a definition of average contact particle eccentricity as such basis. Rorato

125   et al. (2018) suggested instead that a physical measure of grain shape such as sphericity would

126   offer a good basis to calibrate rolling resistance. Herein, this latter idea is developed in detail and

127   tested with several sands.

2 Methodology

2.1 Contact rolling resistance model

This work is based on the Iwashita & Oda contact model (1998) as implemented in the commercial DEM software PFC3D V5 (Itasca Consulting Group Inc. 2014), which has been used for all the simulations presented here. The model is schematically illustrated in Figure 2a, it includes a conventional linear elastic – frictional contact model for particle relative displacement at the contact plus an additional set of elastic spring no-tensional joint and slider for the rolling motion.
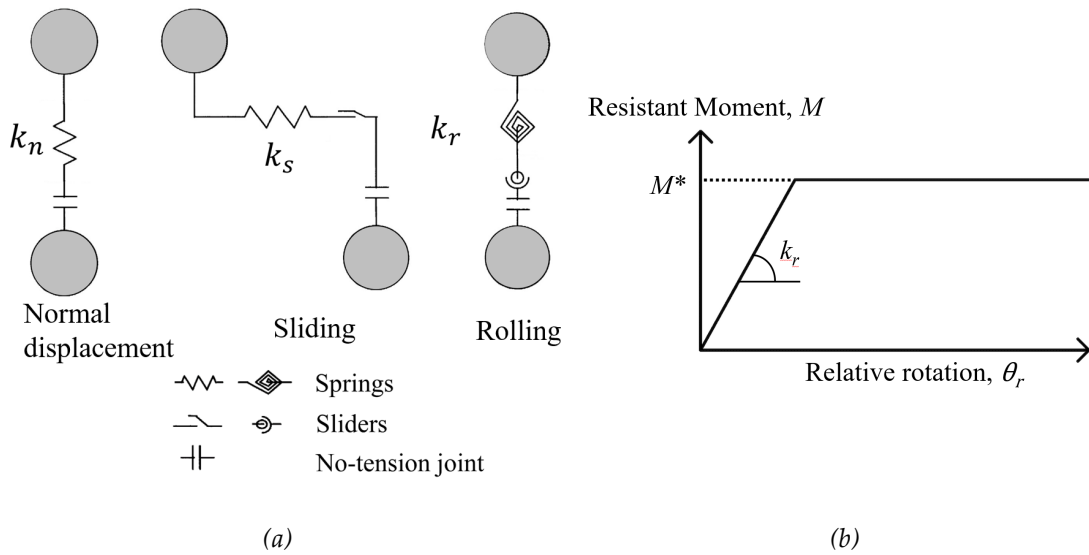

(a) *(b)*

Figure 2: Rolling resistance contact model (a) and elastic-perfectly plastic model accounting for rolling resistance at contact (b).

The contact normal and shear stiffness are defined as

$$k_n = \frac{A E_{mod}}{L} \; ; \; k_s = \frac{k_n}{k_{ratio}} \qquad (1)$$

where E_{mod} and k_{ratio} are material parameters to be calibrated, A is the diameter of the smallest contacting sphere and L is the distance between grain centres. This formulation guarantees scale-invariance of the interaction law (Feng & Owen, 2014).

142   For the moment rotation law (Figure 2b) the following assumptions are used

143   (1) The *rolling stiffness* (k_r) is defined as:

$$k_r = k_s R^2 \qquad (2)$$

144   where k_s is the contact *shear stiffness* and R the *effective radius* defined as

$$R = \frac{1}{R_1} + \frac{1}{R_2} \qquad (3)$$

145   with R_1 and R_2 being the radii of the two particles in contact. The proportionality of rolling and

146   shear stiffness was derived by Iwashita & Oda (1998) to make identical the elastic moment due

147   to shear and that due to rotation. Wensrich & Katterfield (2012) compared this formulation of

148   rolling stiffness with available alternatives and noted that the Iwashita-Oda approach has some

149   numerical advantages as a) it dampens elastic oscillations without the need to introduce extra

150   parameters and b) simplifies the computation of critical time steps.

151   (2) The moment-rotational contact law is implemented as an elastic-perfectly plastic model with

152   the yielding moment (M^*) defined as:

$$M^* = \mu_r F_n R \qquad (4)$$

153   where μ_r is defined as *rolling friction coefficient* and F_n is the normal contact force. The rolling

154   resistance part of the contact model used in this study is illustrated in Figure 2b.

155

156   The Iwashita and Oda (1998) original formulation also includes viscous dissipation at the contact.

157   Wensrich and Katterfeld (2012) showed that the effect of rotational contact viscosity on simula-

158   tion outcomes is negligible for the quasi-static conditions with low inertial numbers which are of

159   interest here. Therefore, viscous dissipation at the contact was not included in the models for

160   simplicity.

2.2 Shape description

The *degree of true sphericity*, ψ (Wadell 1932) is employed to describe grain shape. ψ is defined as

$$\psi = \frac{s_n}{S} = \frac{\sqrt[3]{36\pi V^2}}{S} \qquad (5)$$

where (S) is the particle surface area and (s_n) is the surface area of a sphere with the same volume (V) as the particle. As argued by Rorato et al. (2019a), ψ offers a compact, easy to interpret, and conceptually sound measure of how similar a given particle is to a sphere.

Despite its conceptual simplicity, this shape descriptor had seen relatively little use because measuring the surface area of irregular sand grains is difficult. This has changed in recent years, as computer-based 3D image analysis techniques made such measurements possible. Still, access to 3D imaging equipment is sometimes limited, and 2D images are much easier to acquire and process. For this reason a number of 2D proxy measures of sphericity have been proposed over the years (Rorato et al. 2019a) In this work we use *2D perimeter sphericity S_P. S_P* which is defined as the ratio of the perimeter of the circle with area equal to that projected by the particle to the perimeter of the actual particle projection. Note that we use oriented particle projection – i.e., the projection is made against the plane of maximum particle stability.

2.3 Relating rolling resistance and particle shape

Rorato et al. (2018) hypothesized that the *degree of true sphericity* may be univocally related with a *coefficient of rolling friction*, through a relation such as

$$\mu_r = F(\psi) \qquad (6)$$

This kind of relation maps a physical measured sand property into a discrete element property. Such mapping may be made just on the average value of sphericity, to obtain a single value of

181 rolling resistance to apply for all particles in a DEM model of such sand. However, when an

182 experimental distribution of ψ such as those in Figure 3 is available, the process can be also made

183 element by element, assigning to each one a sampled value from the measured distribution of ψ

184 and then applying the mapping function to initialize its rolling friction coefficient. In this way,

185 the variability in grain shape distribution is directly reflected in the numerical model through a

186 distribution of particle *rolling friction coefficient*.

187

188 Because rolling friction is a contact property, an extra rule is necessary to assign rolling resistance

189 to a contact between two particles. The solution to avoid this ambiguity is to select the minimum,

190 as

$$\mu_r = min\ (\mu_{r,1}\ ,\ \mu_{r,2}) \tag{7}$$

191 where $\mu_{r,1}$ and $\mu_{r,2}$ are the rolling friction coefficients of the two contacting spheres. This is the

192 same rule that the PFC code applies to the sliding friction coefficient when two bodies of different

193 materials contact. Thus, the rolling resisting yielding moment (M^*) varies at each contact depend-

194 ing on (1) the radii of the contacting spheres, that is the *effective radius*, R, (2) the normal contact

195 force F_n and (3) the *coefficient of rolling friction*, different for each contact (from Eqs. 6-7).

196 3 Model calibration

197 3.1 Target experimental data

198 Two natural sands with very different particle shape were selected for calibration: Hostun sand,

199 very angular, and Caicos ooids, very spherical (see Table 1, where physical properties for these

200 sands are reported alongside those of sands later used in validation). A triaxial test campaign on

201 various specimens of Hostun sand and Caicos ooids was performed by Andò (Andò 2013) at

202   Laboratoire 3SR (Grenoble). Systematic tomographic acquisition was carried out throughout.

203   Two tests on dense Hostun sand (specimen "HNEA01") and Caicos ooids (specimen "COEA04")

204   under 100 kPa confining pressure were selected for the calibration. The macroscopic stress strain

205   and volumetric responses recorded in these tests are shown in Figure 4.

	D_{50}	C_u	C_c	G_S	e_{min}	e_{max}	Mineralogy
Hostun	338 μm	1.41	0.95	2.65	0.605	0.927	Quartz
Caicos	420 μm	1.39	1.09	2.80*	-	-	Aragonite (96%) Calcite (3%)
Ottawa	310 μm	1.31	0.95	2.65	0.499	0.850	Quartz
Ticino	540 μm	1.60	2.32	2.68	0.582	0.934	Feldspar (65%) Quartz (30%)

206   *Table 1: Physical properties of the different sands used for calibration and/or validation [D_{50} = mean grain*

207   *size, C_u = Coefficient of uniformity, C_c = Coefficient of curvature, G_S = Specific gravity, e_{min}/ e_{max} = Min-*

208   *imum/maximum void ratio]. Data for Hostun from (Combe 1998), data for Caicos from (Andò 2013), data*

209   *for Ottawa from (Lee et al. 2007), data for Ticino from (Jamiolkowski et al. 2003). * = typical value for*

210   *carbonate sands.*

211   Rorato et al. (2019a) examined the tomographic images of the Hostun HNEA01 and Caicos

212   COEA04 specimens to acquire three-dimensional shape properties (*e.g.*, volume, surface area,

213   lengths, etc.) of every grain. One of the results thus obtained were statistical distributions of ψ

214   for Hostun and Caicos sands (Figure 3). Another important finding from that work was that, in

215   the Hostun and Caicos grains, 3D true sphericity (ψ) showed good linear correlation with the

216   much easier to measure 2D perimeter sphericity S_P. The correlation obtained is given by
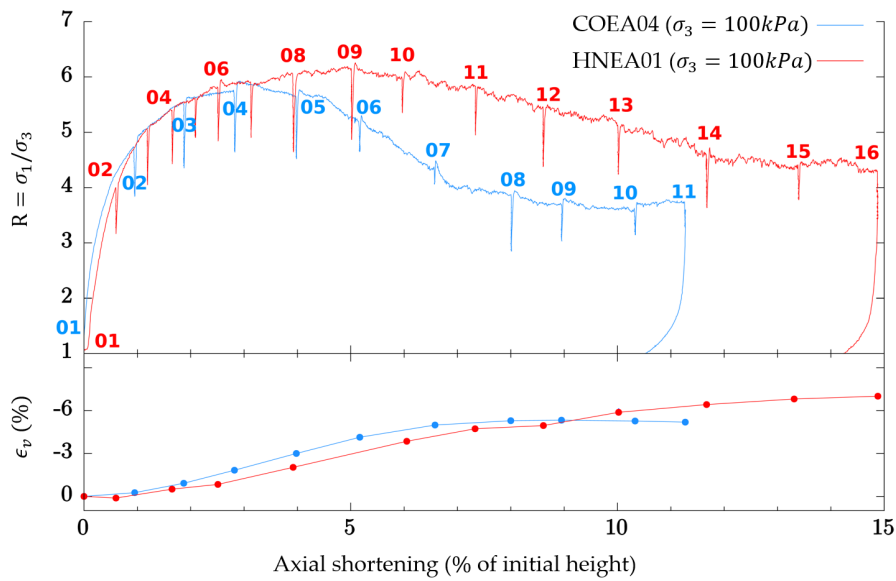
$$\psi = 1.075(S_P) - 0.067 \qquad (8)$$

217

218
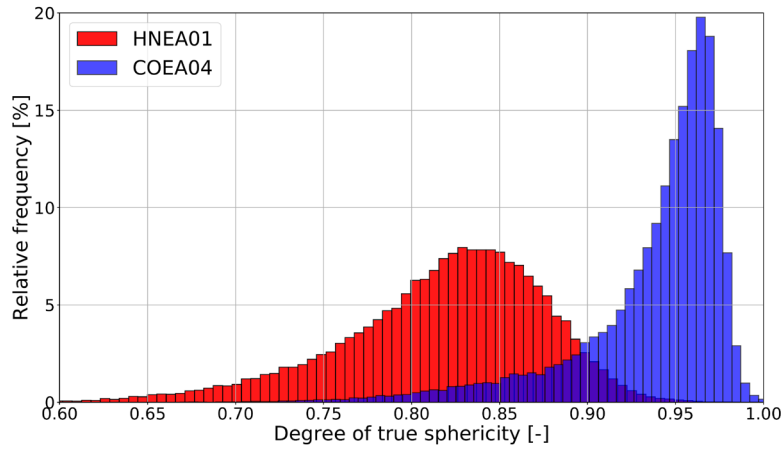
Figure 3: Statistical distribution of the degree of true sphericity of Caicos (COEA04) and Hostun

(HNEA01) sands (Rorato et al. 2019a).

221

222

Figure 4: Triaxial stress-volumetric-strain responses of Hostun sand (specimen HNEA01) and Caicos sand

(specimen COEA04)

A different set of analyses of the scanning data from these two specimens was made to obtain a

database of grain motions. In that work (see Rorato et al. 2020; Rorato, 2019b) Discrete Digital

Volume Correlation (D-DVC, see Hall et al. 2010) is used to obtain the kinematical history of each

sand grain in these triaxial specimens. Averaging that grain scale result for a selection of grains

it is possible to obtain the average grain kinematics in a particular zone of the specimen. Because

230   the specimens failed in a localized shear mode, there was interest in separating the behaviour

231   inside and outside the shear bands. To individuate the grains belonging to the shear band, a nom-

232   inal strain (called "*micro-strain*") was assigned to each grain. That was done – following Catalano

233   et al. (2014) – by means of a Voronoi-based allocation of spatial domains centred around each

234   particle. Once micro-strains are computed, a threshold shear strain value (0.1 in this study) is

235   used to separate the particles that belong to the shear band from those that are outside of it. As a

236   result of this work the average cumulative rotation for the grains in these specimens can be plot-

237   ted (Figure 5).
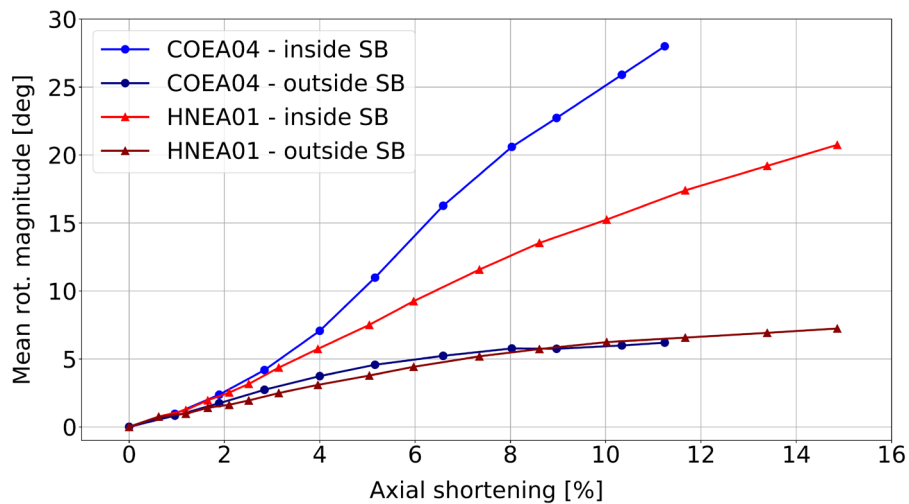
238

239   *Figure 5: Average cumulative rotation of sand grains inside and outside the shear band (Rorato, 2019b).*

240   A further result form that previous work of interest here involves correlations between individual

241   grain shape descriptors and grain rotations . The study (Rorato et al. 2020; Rorato, 2019b) showed

242   that ψ is one of the shape descriptors that best correlated with cumulative grain rotation, partic-

243   ularly for grains that are inside the shear bands.

3.2 Mapping function

245   A monotonically increasing mapping function, $F(\psi)$, seems reasonable, as it provides low values

246   of rolling friction when grain sphericity is high, and vice-versa. Rolling friction values used in

247   previous studies usually range between 0 and 1, although some researchers (*e.g.,* Hosn et al. 2017)

248   have explored higher values. True sphericity ψ has a relatively narrow range in practice. A cube,

249   for instance, has a value of ψ=0.81; detailed examination shows that grain ψ values below 0.6 in

250   Figure 3 likely result from image segmentation errors (Rorato et al., 2019a).

251

252   In a first approximation it may seem tempting to assume a zero value of μ_r for a sphere (ψ=1).

253   However, such assumption has a serious limitation, as the rolling resistance of spherical particles

254   may be significant due to mechanisms such as contact deformation (Jiang et al. 2005) and/or sur-

255   face interlocking due to contact roughness (Huang et al. 2017). It is thus preferable to allow for a

256   finite value of μ_r at the upper limit of sphericity. The mapping function selected for calibration

257   takes then an exponential form

$$\mu_r = A \; (\psi)^{-b} \qquad\qquad (9)$$

3.3 Calibration procedure

259   The parameters of the contact model available for fitting are thus E_{mod} , k_{ratio} and contact sliding

260   friction μ. Apart from that, the two parameters of the sphericity to rolling resistance mapping

261   function, *A* and *b* also require calibration.

262

263   This set of parameters was calibrated, by trial and error, to adjust not only the specimen scale

264   macroscopic response illustrated in Figure 4, but also the observed evolution of average rotation

265   within the shear bands reported in Figure 5. This rotation evolution was included as the macro-

266   scopic stress-strain information does not offer enough information on the particle rolling behav-

267   iour that is directly related to rotational resistance in DEM. In principle, the contact model pa-

268   rameters may be different for each sand, as they are presumed to reflect grain properties not

269   explicitly accounted for in the model, such as mineralogy or roughness. On the other hand, the

13

270   sphericity-rolling resistance mapping function parameters are presumed to be unique for all

271   sands as the function already incorporates the effect of different sand grain shapes.

272   DEM cylindrical specimens were prepared to be tested in triaxial compression. The specimens

273   matched the particle size distribution (PSD) of the actual specimens. The small size of the tested

274   specimens (10mm diameter and 20mm height) made scaling unnecessary, and the numerical

275   specimens maintained the same scale as the experiments. Doing so, the initial models contain

276   about 60.000 particles, close to the number of sand grains identified inside specimens HNEA01

277   and COEA04. To attain prescribed initial conditions of density and pressure arbitrarily low initial

278   friction coefficients (μ_0) were used to facilitate specimen formation after seeding. The specimens

279   were then isotropically compressed up to 100kPa.

280

281   The DEM specimens were limited by a cylindrical wall element on the outer periphery and two

282   horizontal walls at the top and bottom. The radius of the horizontal wall was servo controlled

283   during loading to maintain a constant pressure. During shearing a constant vertical velocity is

284   applied to the top and bottom walls; this velocity was selected to maintain a low inertial number,

285   *I*, which is defined as (Da Cruz et al. 2005):

$$I = \frac{\dot{\gamma} D_{50}}{\sqrt{P/\rho}} \qquad (10)$$

286   where $\dot{\gamma}$ is the shearing rate, *P* is the pressure level (confining pressure) and ρ is the particles

287   density.

288   The same Voronoi-cell based procedure (Catalano et al. 2014) employed to assign microstrain to

289   grains in the experimental specimens was also applied to the numerical specimens. Grains be-

290   longing to a shear band were identified by the assigned shear strain value attained towards the

291   end of the test. The same microstrain shear threshold value used to analyse the experiments (0.1)

292   was also applied here. For all elements assigned to the shear band, their kinematic history was

293   then analysed to extract individual particle rotations, which were then averaged to compare with

294   the equivalent experimental data.

295

296   The trial and error parameter calibration procedure followed well established heuristics for the

297   linear elasto-plastic model (Butlanska, 2014), with parameter E_{mod} mostly selected to match initial

298   stiffness, k_{ratio} to match initial dilatancy and μ to match peak strength. The mapping function

299   parameters were mostly adjusted to match the average rotation vs strain curves, although they

300   also affected post-peak stress-strain behaviour. After a few rounds of iterations, the responses

301   illustrated in Figure 6, Figure 7 and Figure 8 were considered to offer a satisfactory match to the

302   experiments. These results were obtained using the parameters reported in Table 2 -where the

303   parameters of other sands used in later validation simulations are also included.

Parameter	Symbol	Hostun	Caicos	Ottawa	Ticino
Specimen sizes	$H_C(mm)$	20	20	20	20
(height, diameter)	$D_c(mm)$	10	10	10	10
Effective normal contact stiffness	E_{mod} $(10^8 Pa)$	2.0	2.0	1.5	4.0
Normal-to-shear stiffness ratio	k_{ratio}	2.0	2.0	2.0	2.0
Inter-particle friction coefficient	μ	0.575	0.575	0.450	0.600
Degree of true sphericity	ψ	(Fig. 13)	(Fig. 13)	(Fig. 13)	(Eq. 8)
Rolling friction coefficients	μ_r	(Eq. 11)	(Eq. 11)	(Eq. 11)	(Eq. 11)
Rolling stiffness	k_r	(Eq. 2)	(Eq. 2)	(Eq. 2)	(Eq. 2)
Local damping	*(-)*	0.7	0.7	0.7	0.7

Parameter	Symbol	Hostun	Caicos	Ottawa	Ticino
Ball density	$\rho\ (\frac{kg}{m^3})$	2500	2500	2500	2500
Ball scaling factor	*(-)*	1	1	1	1
Confining pressures	$P\ (kPa)$	• 100 • 300	• 100 • 300	• 100	• 100 • 200 • 300
Inertial number	$I\ (10^{-4})$	4.00	4.74	3.67	6.28

304   *Table 2: Parameters and input variables employed in the DEM simulations*
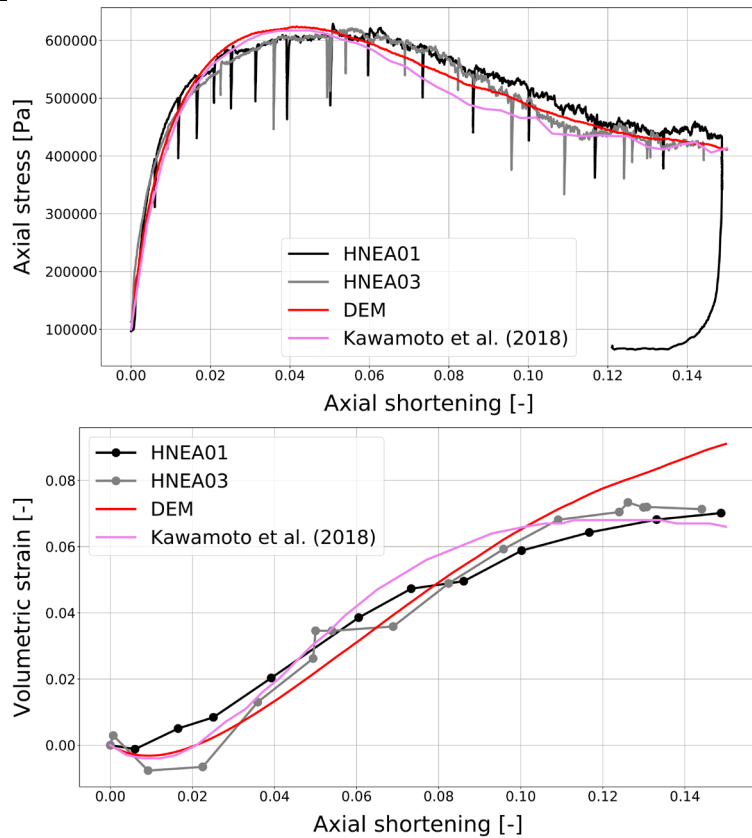

305   *Figure 6: Comparison between the triaxial responses (100kPa confining pressure) of the experiments (spec-*

306   *imens HNEA01 and HNEA03) and the numerical model (DEM) replicating Hostun sand.*

Caicos ooids at 100kPa
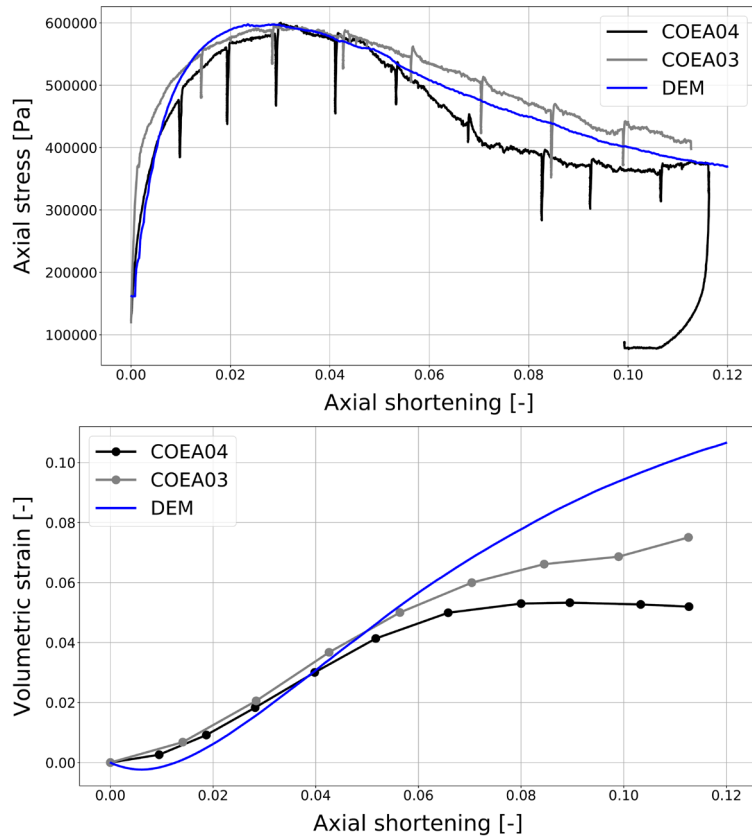
Figure 7: Comparison between the triaxial responses (100kPa confining pressure) of the experiments (specimens COEA03 and COEA04) and the numerical model (DEM) replicating Caicos ooids.
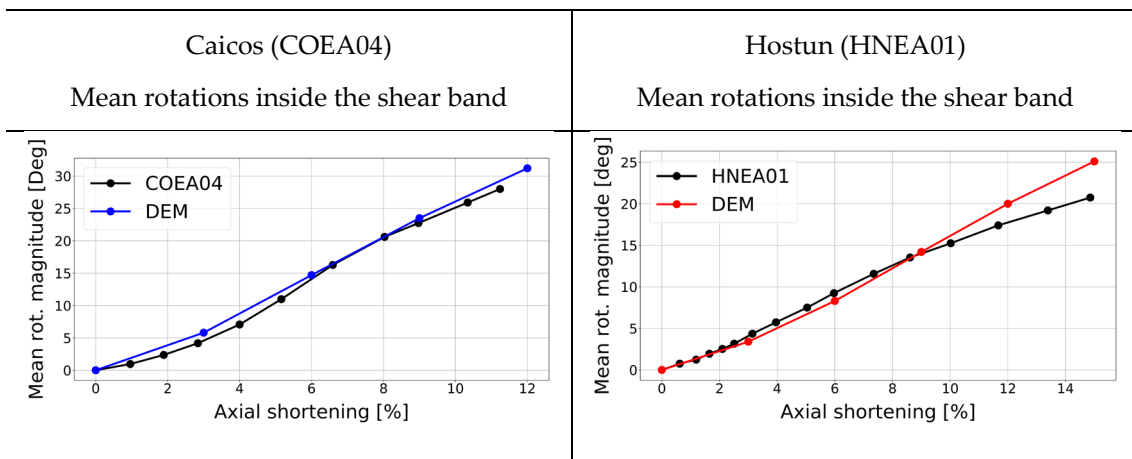

Figure 8: Mean particle rotations for the grains located inside the shear bands (the black grains of Figure 10) for both the experimental and numerical samples, throughout the execution of the triaxial test. The good fit ensures the kinematics at failure is respected.

17

312   Somewhat surprisingly, the adjusted values of the sliding friction coefficients (0.575) and the stiff-

313   ness parameters (effective normal stiffness, stiffness ratio) were identical for both sands. The

314   parameters fitted for the mapping function result in

$$\mu_r = 0.1963(\psi)^{-8.982} \tag{11}$$

315   and this power function is plotted in Figure 9. The calibration result assigns a minimum limiting

316   rolling friction coefficient of about 0.2 to perfectly spherical particles (ψ=1).
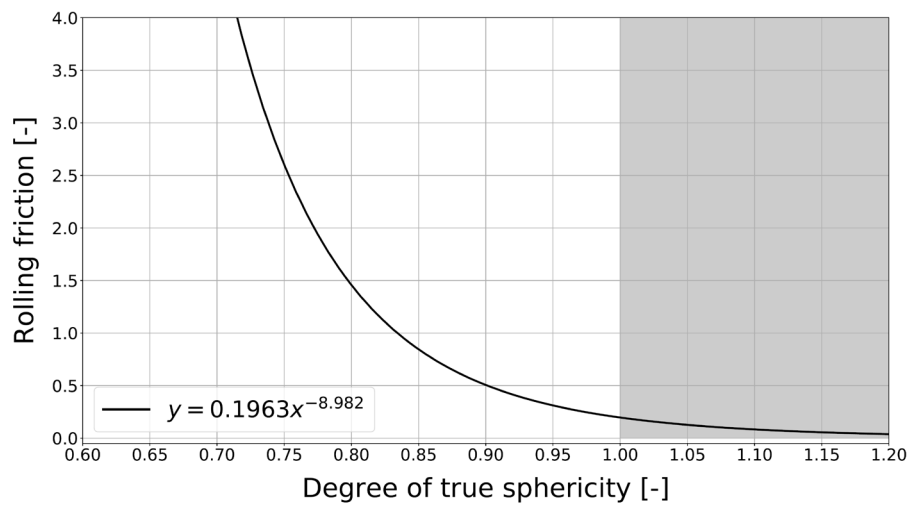
317

318   *Figure 9: Calibrated matching function between particle true sphericity and rolling friction coefficient. The*

319   *shaded area indicates the inadmissible values of true sphericity.*

320   The match obtained for the axial stress-strain behaviour is rather good. Figure 6 and Figure 7 also

321   include results from two experimental replicas of the tests used in calibration, test HNEA03 for

322   Hostun and test COEA03 for Caicos. It can be seen that the numerical results fit well within the

323   baseline experimental variability given by the test replicas.

324   A slight discrepancy is noted in the volumetric vs. axial strain curves. The numerical specimens

325   keep on dilating towards the end when the experimental curves are becoming flat. This is most

326   likely an effect of the simplified model used to represent the cylindrical membrane employed in

327   the physical experiments. The servo controlled external rigid wall employed in the numerical

328   model forces a uniform radial expansion of the specimen, that is particularly unrealistic after

18

329   shear localization takes place. This effect of radial rigid walls on apparent (post localization) di-

330   latancy was recently demonstrated by Khoubany & Evans (2018).

331   Figure 8 shows that an excellent match was attained for the mean particle rotation history inside

332   the shear bands. The overall aspect of the shear bands identified in the numerical simulations is

333   compared with the experimental results in Figure 10. The numerical sample is clearly able to

334   localise the strain, although due to the rigid radial boundary condition applied, the bands are

335   thicker and extend further to the corners. However, the fact that the shear band of Hostun is

336   thicker than that of Caicos (due to increased interlocking effects) indicates that shear band thick-

337   ness variation is qualitatively reproduced in these DEM simulations.

Caicos		Hostun	
Experiment	DEM	Experiment	DEM

(a)   (b)   (c)   (d)
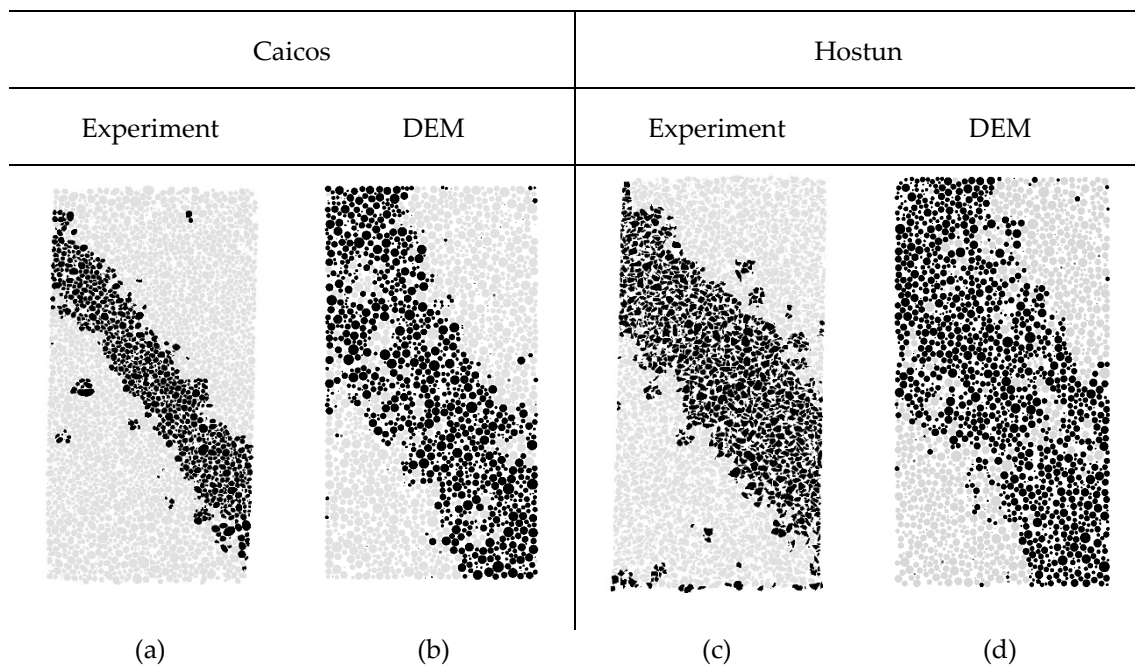
338   *Figure 10: Shear band identification for the experiments and the DEM simulation for both sands (specimens*

339   *HNEA01 and COEA04). Physical (a-c) and numerical (b-d) particles are coloured black if they belong to*

340   *the shear band. The same threshold separates the grains from both sands and both physical and numerical*

341   *samples.*

4 Model validations

4.1 Further tests on Hostun and Caicos sands

The experimental dataset used for calibration was part of a larger triaxial testing campaign, as described by (Andò 2013). That campaign included other triaxial tests on dense Hostun and Caicos specimens at higher confining pressures (300 kPa). Such tests offered a first suitable target for validation.

Numerical specimens identical to those described before were created, trying to approximate the initial porosities (before shearing) of the physical specimens as much as possible (Table 3). The specimens were compressed isotropically to 300kPa and then sheared in triaxial condition until failure was attained. For each sand, all contact properties remain the same as in the 100kPa confining case. The mapping function applied to assign rolling resistance to the elements is also the same.

Sand	Specimen	Relative density (EXP)	Confining pressure	Initial porosity (EXP)	Initial porosity (DEM)
-	-	$D_R(\%)$	(KPa)	$n_{0,exp}(\%)$	$n_{0,DEM}(\%)$
Hostun	HNEA01	83	100	39.7	39.0
Hostun	HNEA02	95	300	38.2	38.6
Caicos	COEA04	-	100	31.9	33.2 (*)
Caicos	COEA02	-	300	33.2	34.3 (*)
Ottawa	OUEA04	112	100	31.4	34.1 (*)
Ticino	TC1	47	109	43.5	44.1
Ticino	TC2	46	200	43.7	43.0
Ticino	TC3	41	300	44.1	43.8
Ticino	TC4	72	100	40.5	39.8
Ticino	TC5	74	200	40.3	39.7
Ticino	TC6	75	300	40.1	40.2
Ticino	TC7	90	100	38.2	38.2
Ticino	TC8	93	200	37.8	38.4
Ticino	TC9	93	300	37.8	37.6

355 *Table 3: Drained triaxial compression tests performed in this study. The relative density and porosity of*

356 *each experimental/numerical test are reported. The symbol (*) means that a denser specimen could not be*

357 *generated for the DEM simulation.*

358 Figure 11 and Figure 12 show the stress-strain-volumetric response of the numerical and experi-

359 mental tests. The numerical curves compare well with the experiments, except for the volumetric

360 dilation of the Caicos specimen, which is again overestimated. This may be partly due to the

361 boundary effects induced by the rigid lateral wall on the post-localization response. Another ef-

362 fect at play may be breakage and/or particle abrasion at this higher stress level. Even small

363 amounts of particle breakage can have a significant effect on dilatancy (Ciantia et al. 2019b).

Hostun sand at 300kPa
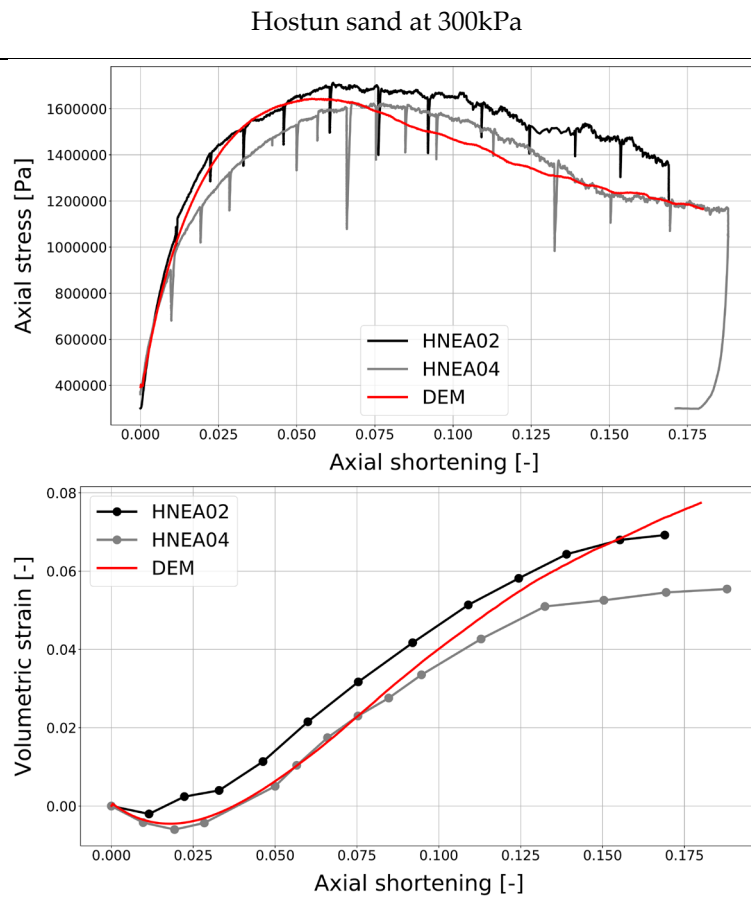
364 *Figure 11: Comparison between the triaxial responses (300kPa confining pressure) of the experiments*

365 *(specimens HNEA02 and HNEA04) and the numerical model (DEM) replicating Hostun sand.*

Caicos ooids at 300kPa
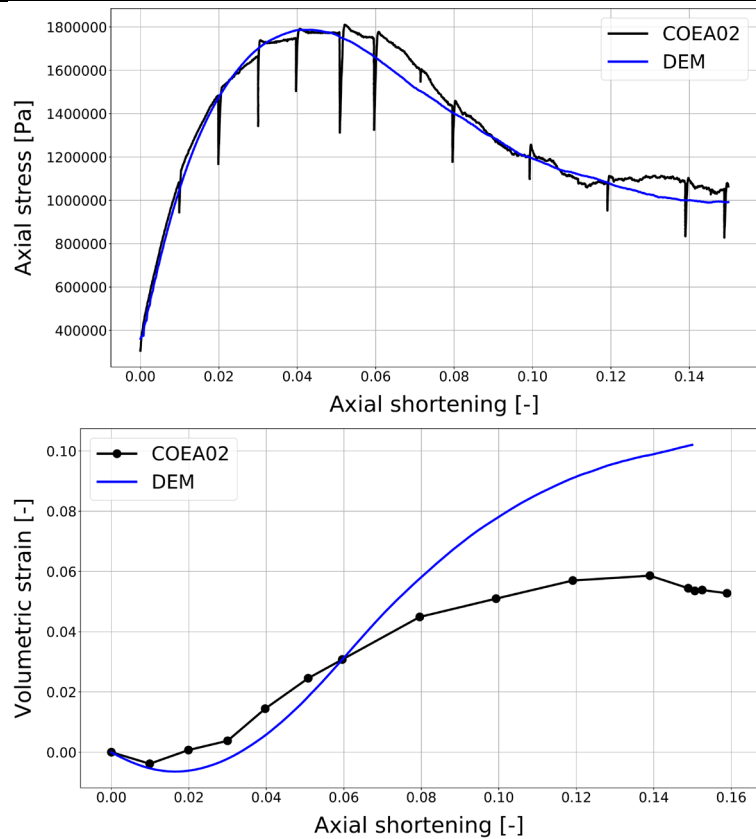
Figure 12: Comparison between the triaxial responses (300kPa confining pressure) of the experiment (specimen COEA02) and the numerical model (DEM) replicating Caicos ooids.

4.2 Triaxial test on Ottawa sand

The experimental campaign by Andò (2013) also included tests in a different silica sand: Ottawa 50/70, which is also a material frequently used in geotechnical research (Table 1). The tests performed at 100 kPa (OUEA04) and 300kPa (OUEA02) were selected for validation. The physical specimen OUEA04 had been scanned using the same tomographic procedures applied for the case of Hostun & Caicos, therefore 3D grain images are available. True sphericity values were computed for all the grains in the specimen (110.000), obtaining the distribution illustrated in Figure 13. The sphericity values of Ottawa peak between those of Caicos and Hostun.

23
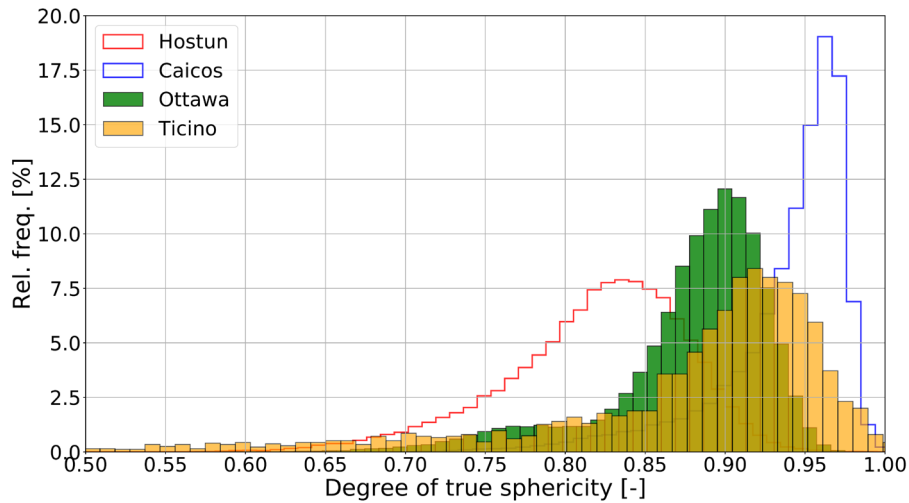
Figure 13: Statistical distributions of 3D true sphericity for Hostun, Caicos, Ottawa and Ticino sands.

The DEM specimens were then prepared matching the experimental PSD and approximating as much as possible the initial porosity (Table 3). The specimens were prepared without scaling, including about 102.000 spherical elements, slightly below the number of grains contained in the physical sample. Specimen preparation and triaxial testing followed identical procedures as those previously described.

In principle, only the contact parameters E_{mod} and k_{ratio} (*i.e.*, k_n and k_s) and coefficient of sliding friction (μ) were free to adjust, as the sphericity to rolling resistance mapping function applied was the same. In practice only E_{mod} and μ were adjusted -- using the test at 100 kPa -- to values of 0.15 GPa and 0.45, respectively. The k_{ratio} value was maintained as 2.0, as in the other sands (Table 2).

Figure 14 and Figure 15 show the comparison between the experimental and numerical results at 100kPa and 300kPa confinement, respectively. The figures include two experimental replicas of the tests, which were also available (OUEA06 and OUEA03, respectively for the 100kPa and 300kPa confinements). The simulations provide a good fit to the experiments; in this case even the post-localization volumetric mismatch is small.

24
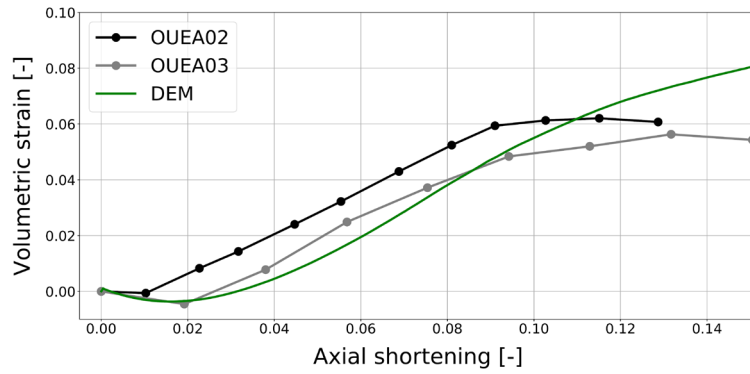
Ottawa sand at 100kPa
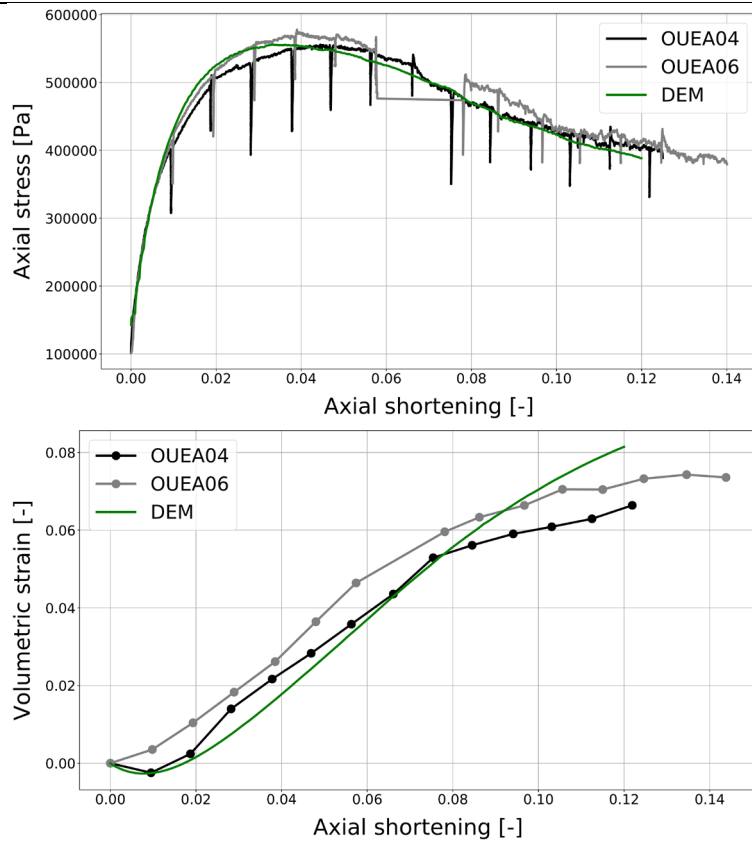
Figure 14: Comparison between the triaxial responses (100kPa confining pressure) of the experiments

(specimens OUEA04 and OUEA06) and the numerical model (DEM) replicating Ottawa sand.

Ottawa sand at 300kPa
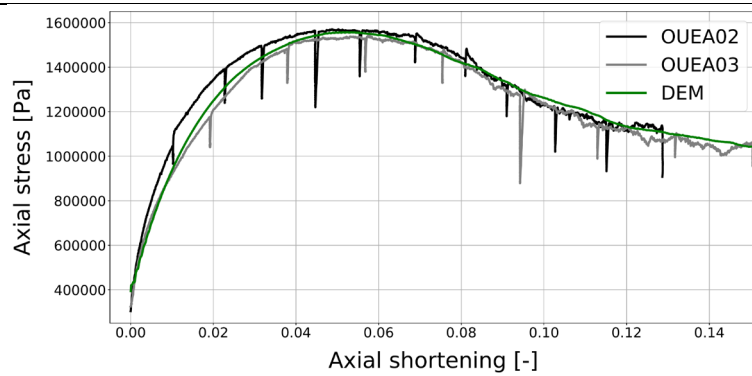
Figure 15: Comparison between the triaxial responses (300kPa confining pressure) of the experiments

(specimens OUEA02 and OUEA03) and the numerical model (DEM) replicating Ottawa sand.

4.3 Triaxial tests on Ticino sand

Ticino sand (Table 1) is a poorly graded medium-sized sand, with grains of medium angularity. The macroscopic responses of Ticino sand have been well reproduced using DEM by several researchers either using clumps (Gotteland et al. 2009) or by inhibiting rotations (Calvetti 2008, Arroyo et al. 2011, Butlanska et al. 2014). Ticino sand will be here modelled using the rolling resistance model with rolling resistance values assigned through the mapping function (Eq. 11).

There were no 3D tomographic images of Ticino sand readily available to establish the sphericity distribution to be input in the mapping function. As an alternative, a table scanner (*CanoScan LiDE 25*) was employed to acquire 2D images of about 4000 grains of Ticino sand. Rorato et al. (2019a) showed that this sample size is enough to obtain a good definition of the sphericity statistics. The table scanner used had 1200 dpi, or equivalently about 20μm/pixel, which is only slightly above the 15μm voxel side used in the 3D μ-CT image acquisition for the other sands. The parallel projection of each grain on the scan surface avoids parallax errors. The scanned image was binarised, segmented and labelled using the open-source python package SPAM (Andò et al. 2017), as shown in Figure 16.

Original image (from scanner)	Labelled image

(a)   *(b)*
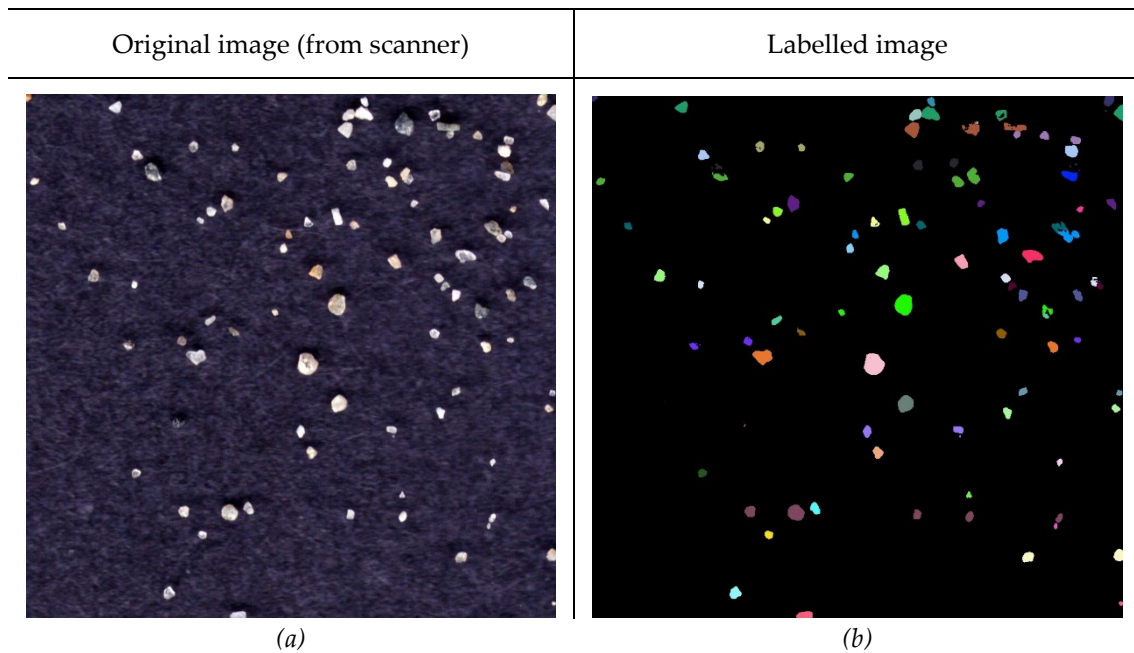
415   *Figure 16: Zoom on (a) the original scan and (b) the labelled image of Ticino sand.*

416   Using a dedicated python script 2D perimeter sphericity was calculated for each grain identified

417   in the image. Equation 8 relating the known 2D perimeter sphericity (S_P) and the 3D true sphe-

418   ricity (ψ) was applied to obtain a statistical distribution of 3D true sphericity. This is plotted in

419   Figure 13: as for Ottawa sand, the mean sphericity of Ticino sand was located between those of

420   Hostun and Caicos sands. It can be noted that the dispersion is higher than for the other sands,

421   with a wide tail of low sphericities. This is likely a side effect of the approximations involved in

422   the 2D procedure.

423

424   DEM triaxial simulations were carried out for a total of nine triaxial tests, including specimens at

425   dense ($D_R \cong 90\%$), medium ($D_R \cong 75\%$) and loose ($D_R \cong 50\%$) states, at variable confining pres-

426   sures (100, 200 and 300kPa). The triaxial chamber used for the DEM simulations kept the same

427   geometry as that employed for Caicos, Hostun and Ottawa (Table 2), which – in this case – was

428   much smaller than that employed in the physical experiments. Again, no particle scaling was

429   applied and, due to the larger grain size of Ticino sand, about 16.000 elements were employed in

430   each numerical specimen.

431

432   One specimen (100kPa confining, $D_R \cong 75\%$) was selected to calibrate contact parameters

433   E_{mod} and μ (the k_{ratio} value was kept at 2, as in the other sands). After a few iterations the values

434   finally selected were, respectively, 0.4 GPa and 0.60 (Table 2).

435

436   The mechanical responses (stress-strain-volumetric) of the nine DEM simulations are shown

437   alongside the corresponding experimental results in Figure 17 ($D_R \cong 50\%$), Figure 18 ($D_R \cong 75\%$)

438   and Figure 19 ($D_R \cong 90\%$). It is evident that the triaxial response is well reproduced under all

439   stress and state conditions used in the tests. Small discrepancies can be seen for the DEM simula-

440   tions at 300kPa but it must be mentioned that some particle crushing - not modelled here - was

441   noted in the physical samples at the end of those tests.

442   This case strongly suggests that there is no need to have a full three-dimensional tomographic

443   identification of sand grain shapes. Thanks to the good correlation between true sphericity and

444   2D perimeter sphericity (equation 8), the required rolling resistance for DEM analysis can be

445   readily determined based on the observations of 2D images.
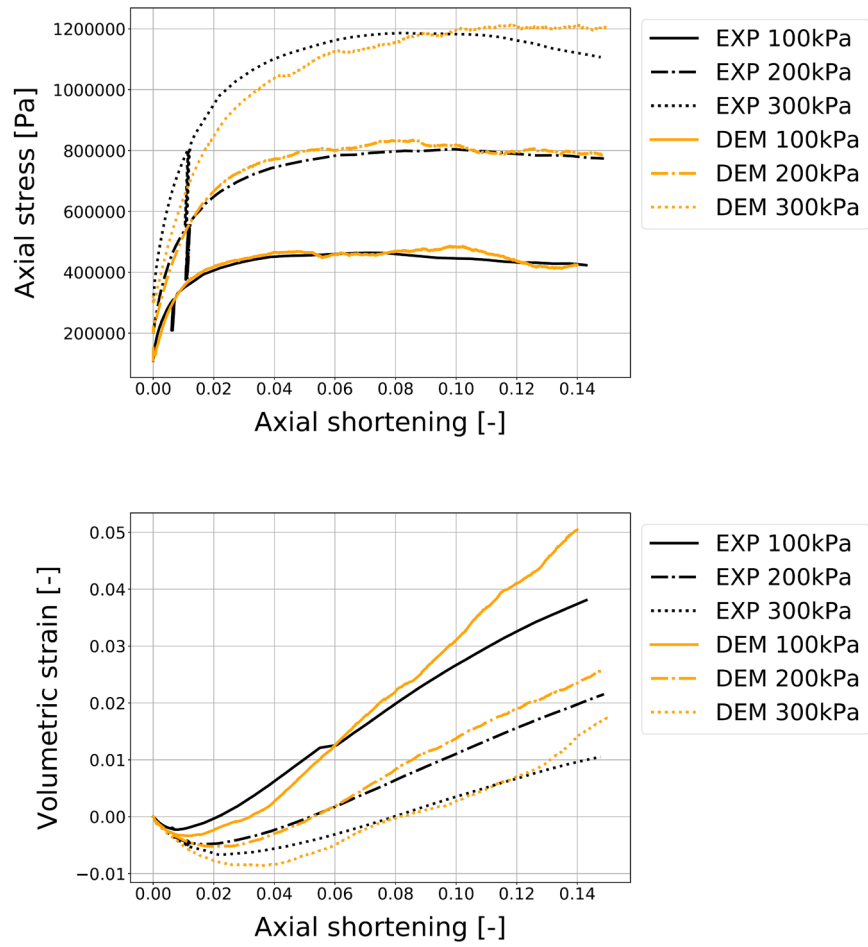
446   *Figure 17: Triaxial responses of loose Ticino sand at 100-200-300kPa*
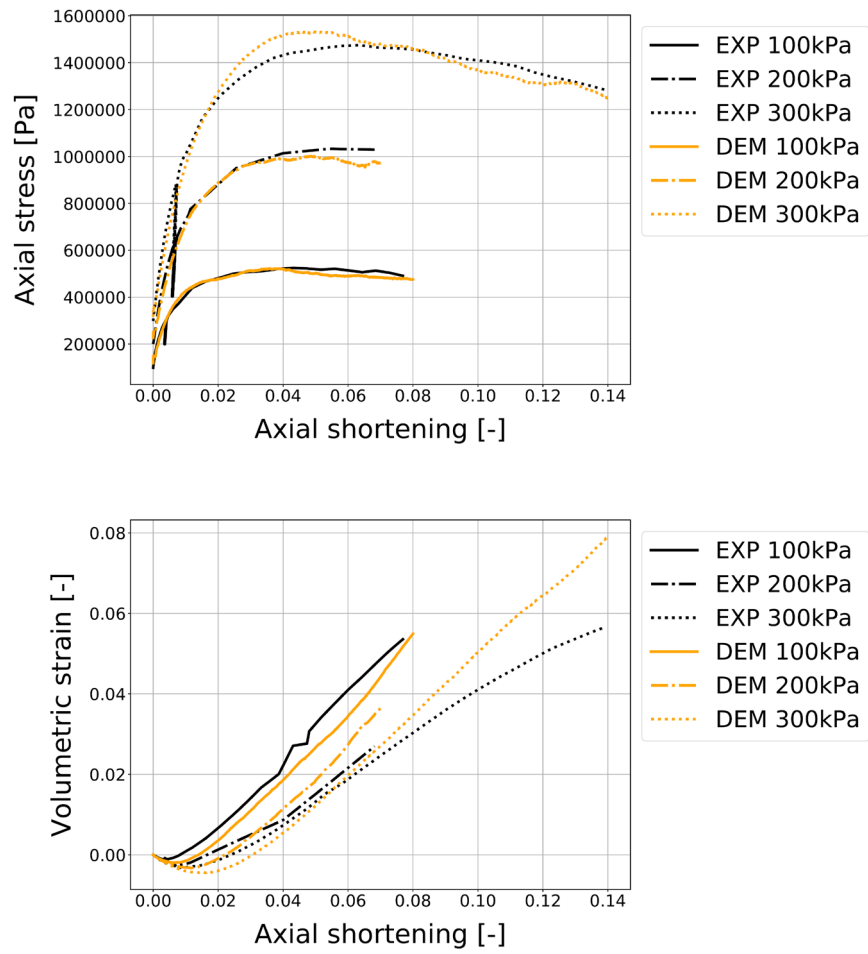
447   *Figure 18: Triaxial responses of medium Ticino sand at 100-200-300kPa*

Dense state ($D_R \cong 90\%$)
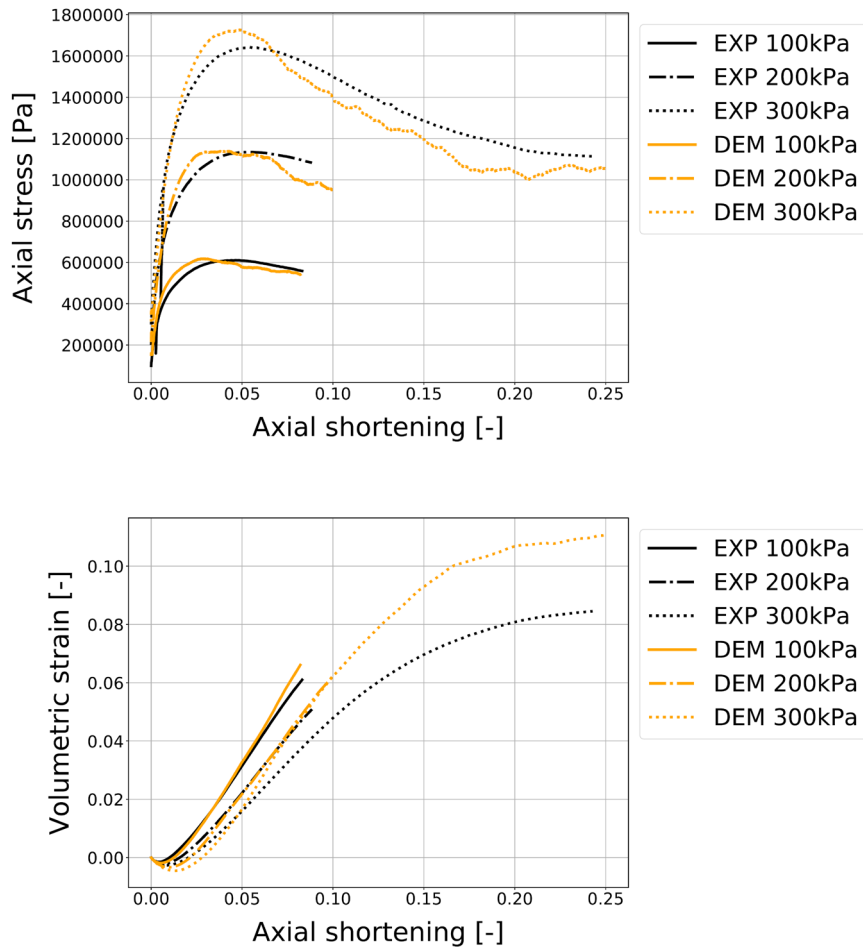
Figure 19: Triaxial responses of dense Ticino sand at 100-200-300kPa

5 Discussion

A comparison can be made with the approach proposed by Wensrich & Katterfeld (2012), who,

based on geometric deductive reasoning, suggested that rolling resistance could be evaluated as

the ratio of grain surface – averaged contact eccentricity $\langle e \rangle$ and the equivalent grain radius (*i.e.,*

the radius of a sphere with equal volume as the grain), R_{eq}

$$\mu_r = \frac{\langle e \rangle}{R_{eq}} \qquad (12)$$

454 The rolling friction values evaluated with Eq. 12 are compared with those predicted by Equation

455 11 in Figure 20. The rolling friction values obtained are similar for high sphericity values. Despite

456 this coincidence, it is noted that further work with the average contact eccentricity concept

457 (Wensrich et al. 2014) concluded that values given by Equation 12, should be halved to obtain

458 good matches with clump-based simulations, which would separate further the eccentricity-

459 based rolling friction values from those derived from our proposal. This difference may reflect

460 the decision to represent in our model not just structural rolling resistance - *i.e.*, the one reflected

461 by eccentricity - but also contact-level sources or rolling resistance, allowing non-zero rolling re-

462 sistance for spheres.
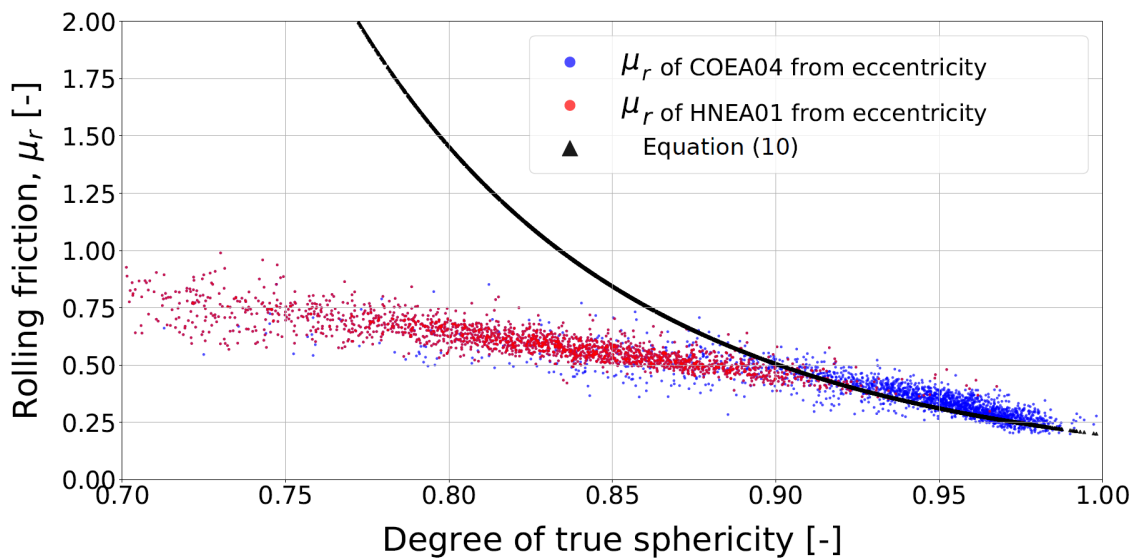
463

464 *Figure 20: Comparison of rolling friction values derived from average eccentricity following Wensrich &*

465 *Katterfeld (2012) and those given by the calibrated mapping function*

466 Another interesting comparison is with the work of Kawamoto (Kawamoto et al. 2018) who built

467 a DEM-based "avatar" of specimen of HNEA01 in which a much higher level of detail of each

468 grain shape was represented, via level sets. The "avatar" approach does not individuate single

469 grains for validation, but, as done here with average shear band rotation, relies on emerging en-

470 semble measures (like shear band orientation) for validation. The simulation results obtained by

471 Kawamoto et al (2018) for Hostun using a level set method to incorporate explicitly grain shape

472 are also included in Figure 6 for comparison. The results are not very different from those ob-

473 tained here, with discrepancies in dilatancy attributable to the much more realistic numerical

474 representation of boundary conditions (loading platens and flexible membrane surrounding the

475 specimen) in the work of Kawamoto et al. (2018). It is also interesting that the sliding friction

476 value that was calibrated (0.575) by Kawamoto et al. (2018) was very close to the one calibrated

477 here (0.55). Of course, the computational cost is very different: while simulating specimen

478 HNEA01 through level set approach took 17 h in the 480 cores of the San Diego Supercomputer,

479 using the model calibrated here a simulation of the same specimen lasts 20h in a four-core desktop

480 computer.

6 Conclusions

482 This paper presents a novel technique to relate univocally the d*egree of true sphericity* of each grain

483 contained in a sand sample with the *coefficient of rolling friction* to apply to its numerical counter-

484 part of spherical shape. This approach greatly simplifies the complex calibration procedure of

485 rolling resistance contact models, easily incorporating information on natural shape variability in

486 the numerical discrete model.

487

488 It has been also shown that easily-acquired 2D proxy measures of sphericity can be used instead

489 of the more difficult to acquire direct 3D measurements. A relatively cheap table scanner may be

490 all that is required to evaluate the coefficient of rolling friction.

491

492 For the four different sands examined, the approach appeared to work successfully using a

493 unique mapping function between true sphericity and rolling friction. However, the validity of

494 the approach has only been tested for triaxial compression paths. with different stress paths

495 seems necessary in this respect. Future work will also explore if the proposed mapping of sphe-

496 ricity into rolling friction holds true when other modelling features are modified, such as the

497 allocation rule for rolling friction at the contact, or the definition of contact stiffness (e.g. by using

498 a Hertzian contact model instead of linear stiffness).

499 **7 Acknowledgments**

503 **8 References**

504 Ai, J., Chen, J.F., Rotter, J.M., and Ooi, J.Y. 2011. Assessment of rolling resistance models in

505   discrete element simulations. Powder Technology, **206**(3): 269–282. Elsevier B.V.

506   doi:10.1016/j.powtec.2010.09.030.

507 Alshibli, K.A., Druckrey, A.M., Al-Raoush, R.I., Weiskittel, T., and Lavrik, N. V. 2015. Quantifying

508   Morphology of Sands Using 3D Imaging. Journal of Materials in Civil Engineering, **27**(10).

509   doi:10.1061/(ASCE)MT.1943-5533.0001246.

510 Alshibli, K.A., Jarrar, M.F., Druckrey, A.M., and Al-Raoush, R.I. 2017. Influence of Particle Mor-

511   phology on 3D Kinematic Behavior and Strain Localization of Sheared Sand. Journal of Ge-

512   otechnical and Geoenvironmental Engineering, **143**(2): 04016097.

513   doi:10.1061/(ASCE)GT.1943-5606.0001601.

514 Andò, E. 2013. Experimental investigation of microstructural changes in deforming granular

515   media using x-ray tomography. PhD Thesis. Université de Grenoble.

516   Andò, E., Hall, S.A., Viggiani, G., Desrues, J., and Bésuelle, P. 2012. Grain-scale experimental in-

517   vestigation of localised deformation in sand: A discrete particle tracking approach. Acta

518   Geotechnica, **7**(1): 1–13. doi:10.1007/s11440-011-0151-6.

519   Andò, E., Cailletaud, R., Roubin, E., Stamati, O., and the spam contributors. 2017. SPAM: The

520   Software for the Practical Analysis of Materials.

521   Arroyo, M., Butlanska, J., Gens, A., Calvetti, F., and Jamiolkowski, M. 2011. Cone penetration tests

522   in a virtual calibration chamber. Geotechnique, **61**(6): 525–531. doi:10.1680/geot.9.P.067.

523   Bardet, J. P. (1994). Observations on the effects of particle rotations on the failure of idealized

524   granular materials. Mechanics of materials, 18(2), 159-182

525   Barret, P.J. 1980. The shape of rock particle, a critical review. Sedimentology, **27**: 291–303.

526   doi:10.1111/j.1365-3091.1980.tb01179.x.

527   Bathurst, R.J., and Rothenburg, L. 1992. Micromechanical features of granular assemblies with

528   planar elliptical particles. Géotechnique, **42**(1): 79–95. doi:10.1680/geot.1992.42.1.79.

529   Belheine, N., Plassiard, J.P., Donzé, F. V., Darve, F., and Seridi, A. 2009. Numerical simulation of

530   drained triaxial test using 3D discrete element modeling. Computers and Geotechnics, **36**(1–

531   2): 320–331. doi:10.1016/j.compgeo.2008.02.003.

532   Boon, C. W., Houlsby, G. T., & Utili, S. (2012). A new algorithm for contact detection between

533   convex polygonal and polyhedral particles in the discrete element method. Computers and

534   Geotechnics, 44, 73-82.

535   Butlanska, J., Arroyo, M., Gens, A., and O'Sullivan, C. 2014. Multi-scale analysis of cone

536   penetration test (CPT) in a virtual calibration chamber. Canadian Geotechnical Journal,

537   **51**(1): 51–66. doi:10.1139/cgj-2012-0476.

538   Butlanska, J. (2014). Cone penetration test in a virtual calibration chamber (Doctoral dissertation,

539   Universitat Politècnica de Catalunya (UPC)).

540   Calvetti, F. 2008. Discrete modelling of granular materials and geotechnical problems. European

541   Journal of Environmental and Civil Engineering, **12**(7–8): 951–965.

542   doi:10.3166/EJECE.12.951-965.

543   Calvetti, F., Viggiani, G., and Tamagnini, C. 2003. A numerical investigation of the incremental

544   behavior of granular soils. Rivista Italiana di Geotecnica, **37**(3): 11–29. Available from

545   http://www.associazionegeotecnica.it/sites/default/files/rig/RIG_2003_3_11.pdf

546   Catalano, E., Chareyre, B., and Barthélémy, E. 2014. Pore-scale modeling of fluid-particles inter-

547   action and emerging poromechanical effects. International Journal for Numerical and Ana-

548   lytical Methods in Geomechanics, **38**(1): 51–71. John Wiley & Sons, Ltd.

549   doi:10.1002/nag.2198.

550   Cavarretta, I., O'sullivan, C., Ibraim, E., Lings, M., Hamlin, S., and Wood, D.M. 2012. Characteri-

551   zation of artificial spherical particles for DEM validation studies. Particuology, **10**: 209–220.

552   doi:10.1016/j.partic.2011.10.007.

553   Cheng, H., Shuku, T., Thoeni, K., & Yamamoto, H. (2018). Probabilistic calibration of discrete

554   element simulations using the sequential quasi-Monte Carlo filter. Granular matter, 20(1),

555   11.

556   Cheng, K., Wang, Y., Yang, Q., Mo, Y., and Guo, Y. 2017. Determination of microscopic parame-

557   ters of quartz sand through tri-axial test using the discrete element method. Computers and

558   Geotechnics, **92**(August): 22–40. Elsevier Ltd. doi:10.1016/j.compgeo.2017.07.017.

559   Ciantia, M.O., Arroyo, M., Calvetti, F., and Gens, A. 2015. An approach to enhance efficiency of

560   DEM modelling of soils with crushable grains. Géotechnique, **65**(2): 91–110.

561   doi:10.1680/geot.13.P.218.

562   Ciantia, M.O., Arroyo, M., O'Sullivan, C., Gens, A., and Liu, T. 2019a. Grading evolution and

563   critical state in a discrete numerical model of Fontainebleau sand. Géotechnique, **69**(1): 1–

564   15. Thomas Telford Ltd. doi:10.1680/jgeot.17.P.023.

565   Ciantia, M. O., Arroyo, M., O'Sullivan, C., & Gens, A. (2019b). Micromechanical inspection of

566   incremental behaviour of crushable soils. Acta Geotechnica, 14(5), 1337-1356.

567   Combe, A.-L. 1998. Comportement du sable d'Hostun S28 au triaxial axisymétrique.

568   Comparaison avec le sable d'Hostun RF. Université Joseph Fourier, Grenoble.

569 Combe, G., and Roux, J.-N. 2003. Discrete numerical simulation, quasistatic deformation and the

570   origins of strain in granular materials. Discrete numerical simulation, quasistatic

571   deformation and the origins of strain in granular materials. *In* 3ème Symposium

572   International sur le Comportement des sols et des roches tendres. Lyon. pp. 1071–1078.

573   Available from https://hal.archives-ouvertes.fr/hal-00354754.

574 Cui, L., and O'Sullivan, C. 2006. Exploring the macro- and micro-scale response of an idealised

575   granular material in the direct shear apparatus. Géotechnique, **56**(7): 455–468.

576   doi:10.1680/geot.56.7.455.

577 Cundall, P.A., and Strack, O.D.L. 1979. A discrete numerical model for granular assemblies.

578   Géotechnique, **29**(1): 47–65. doi:10.1680/geot.1979.29.1.47.

579 Cho, A.G., Dodds, J., and Santamarina, J.C. 2006. Particle Shape Effects on Packing Density ,

580   Stiffness and Strength – Natural and Crushed Sands. Journal of Geotechnical and

581   Geoenvironmental   Engineering,   **132**(5):   591–602.   doi:10.1061/(ASCE)1090-

582   0241(2006)132:5(591).

583 Da Cruz, F., Emam, S., Prochnow, M., Roux, J.N., and Chevoir, F. 2005. Rheophysics of dense

584   granular materials: Discrete simulation of plane shear flows. Physical Review E - Statistical,

585   Nonlinear, and Soft Matter Physics, **72**(2): 1–17. doi:10.1103/PhysRevE.72.021309.

586 Elias, J. 2013. DEM simulation of railway ballast using polyhedral elemental shapes. *In*

587   PARTICLES 2013 - III International Conference on Particle-based Methods – Fundamentals

588   and Applications. Barcelona. pp. 1–10.

589 Estrada, N., Taboada, A., and Radjaï, F. 2008. Shear strength and force transmission in granular

590   media with rolling resistance. Physical Review E - Statistical, Nonlinear, and Soft Matter

591   Physics, **78**(2): 1–11. doi:10.1103/PhysRevE.78.021301.

592 Fonseca, J., O'Sullivan, C., Coop, M.R., and Lee, P.D. 2012. Non-invasive characterization of par-

593   ticle morphology of natural sands. Soils and Foundations, **52**(4): 712–722. Elsevier.

594 doi:10.1016/j.sandf.2012.07.011.

595 Feng, Y. T., & Owen, D. R. J. (2014). Discrete element modelling of large scale particle systems—

596 I: exact scaling laws. Computational Particle Mechanics, 1(2), 159-168.

597 Gotteland, P., Villard, P., Salot, C., Nakagawa, M., and Luding, S. 2009. Using Nonconvex

598 Discrete Elements to Predict Experimental Behaviour of Granular Materials. *In* Proceedings

599 of the 6th International Conference on Micromechanics of Granular Media. AIP. pp. 361–

600 364. doi:10.1063/1.3179934.

601 Hall, S.A., Bornert, M., Desrues, J., Pannier, Y., Lenoir, N., Viggiani, G. & Bésuelle, P. (2010) Dis-

602 crete and continuum analysis of localised deformation in sand using X-ray μCT and volu-

603 metric digital image correlation. Géotechnique. 60 (5), 315–322.

604 Hosn, R. A., Sibille, L., Benahmed, N., & Chareyre, B. (2018). A discrete numerical model involv-

605 ing partial fluid-solid coupling to describe suffusion effects in soils. Computers and Ge-

606 otechnics, 95, 30-39.

607 Huang, X., Hanley, K. J., O'Sullivan, C., & Kwok, C. Y. (2017). Implementation of rotational re-

608 sistance models: a critical appraisal. Particuology, 34, 14-23.

609 Itasca Consulting Group Inc. 2014. PFC — Particle Flow Code, Ver. 5.0. Minneapolis: Itasca.

610 Available from https://www.itascacg.com/software-faq.

611 Irazábal, J., Salazar, F., & Oñate, E. (2017). Numerical modelling of granular materials with spher-

612 ical discrete particles and the bounded rolling friction model. Application to railway ballast.

613 Computers and Geotechnics, 85, 220-229.

614 Iwashita, K., and Oda, M. 1998. Rolling resistance at contacts in simulation of shear band

615 development by DEM. Journal of Engineering Mechanics, **124**(3): 285–292.

616 doi:10.1061/(ASCE)0733-9399(1998)124:3(285).

617 Iwashita, K., and Oda, M. 2000. Micro-deformation mechanism of shear banding process based

618 on modified distinct element method. Powder Technology, **109**(1–3): 192–205.

619 doi:10.1016/S0032-5910(99)00236-3.

620 Jamiolkowski, M., Lo Presti, D.C.F., and Manassero, M. 2003. Evaluation of Relative Density and

621   Shear Strength of Sands from CPT and DMT. *In* Symposium on Soil Behavior and Soft

622   Ground Construction Honoring Charles C. "Chuck" Ladd. Cambridge, USA.

623   doi:10.1061/40659(2003)7.

624 Jerves, A.X., Kawamoto, R.Y., and Andrade, J.E. 2016. Effects of grain morphology on critical

625   state: A computational analysis. Acta Geotechnica, **11**(3): 493–503. doi:10.1007/s11440-015-

626   0422-8.

627 Jiang, M.J.J., Yu, H.-S., and Harris, D. 2005. A novel discrete model for granular material

628   incorporating rolling resistance. Computers and Geotechnics, **32**(5): 340–357.

629   doi:10.1016/j.compgeo.2005.05.001.

630 Katagiri, J., Matsushima, T., Yamada, Y., Katagiri, J., Matsushima, T., and Yamada, Y. 2010.

631   Simple shear simulation of 3D irregularly-shaped particles by image-based DEM. Granular

632   Matter, **12**: 491–497. doi:10.1007/s10035-010-0207-6.

633 Kawamoto, R., Andò, E., Viggiani, G., and Andrade, J.E. 2018. All you need is shape: Predicting

634   shear banding in sand with LS-DEM. Journal of the Mechanics and Physics of Solids, **111**:

635   375–392. Elsevier Ltd. doi:10.1016/j.jmps.2017.10.003.

636 Kawano, K., Shire, T., & O'Sullivan, C. (2018). Coupled particle-fluid simulations of the initiation

637   of suffusion. Soils and foundations, 58(4), 972-985.

638 Khoubani, A., & Evans, T. M. (2018). An efficient flexible membrane boundary condition for DEM

639   simulation of axisymmetric element tests. International Journal for Numerical and Analyti-

640   cal Methods in Geomechanics, 42(4), 694-715.

641 Kong, D., and Fonseca, J. 2018. Quantification of the morphology of shelly carbonate sands using

642   3D images. Géotechnique, **68**(3): 249–261. doi:10.1680/jgeot.16.P.278.

643 Krumbein, W.C. 1941. Measurement and Geological significance of shape and roundness of sed-

644   imentary particles. Journal of Sedimentary Petrology, **11**(2): 64–72.

645 Langston, P., Ai, J., and Yu, H.-S. 2013. Simple shear in 3D DEM polyhedral particles and in a

646   simplified 2D continuum model. Granular Matter, **15**: 595–606. doi:10.1007/s10035-013-

647   0421-0.

648 Lee, J.-S., Dodds, J., and Santamarina, J.C. 2007. Behavior of Rigid-Soft Particle Mixtures. Journal

649   of Materials in Civil Engineering, **19**(2): 179–184. doi:10.1061/(ASCE)0899-1561(2007)19.

650 Li, T., Jiang, M., & Thornton, C. (2018). Three-dimensional discrete element analysis of triaxial

651   tests and wetting tests on unsaturated compacted silt. Computers and Geotechnics, 97, 90-

652   102.

653 Lin, X., & Ng, T. T. (1997). A three-dimensional discrete element model using arrays of ellipsoids.

654   Geotechnique, 47(2), 319-329.

655 Liu, Q.B., and Lehane, B.M. 2013. The influence of particle shape on the (centrifuge) cone

656   penetration test (CPT) end resistance in uniformly graded granular soils. Géotechnique,

657   **60**(2): 111–121. doi:10.1139/t06-037.

658 Lu, M., and McDowell, G.R. 2007. The importance of modelling ballast particle shape in the

659   discrete element method. Granular Matter, **9**(1–2): 69–80. doi:10.1007/s10035-006-0021-3.

660 Lu, G., Third, J. R., & Müller, C. R. (2015). Discrete element models for non-spherical particle

661   systems: from theoretical developments to applications. Chemical Engineering Science, 127,

662   425-465.

663 Matsushima. 2002. Discrete Element Modeling for Irregularly-Shaped Sand Grains. La

664   Modélisation aux Éléments Discrets d'un sable a grains de forme irrégulière (1998): 239–246.

665 Midi, G. 2004. On dense granular flows. Eur. Phys. J. E, **14**: 341–365. doi:10.1140/epje/i2003-10153-

666   0.

667 Mohamed, A., & Gutierrez, M. (2010). Comprehensive study of the effects of rolling resistance on

668   the stress–strain and strain localization behavior of granular materials. Granular Matter,

669   12(5), 527-541.

670 Ng, T.T. 1994. Numerical simulations of granular soil using elliptical particles. Computers and

671   Geotechnics, **16**(2): 153–169. doi:10.1016/0266-352X(94)90019-1.

672 O'Sullivan, C., Riemer, M.F., Bray, J.D., and Riemer, M. 2004. Examination of the Response of

673   Regularly Packed Specimens of Spherical Particles Using Physical Tests and Discrete Ele-

674   ment Simulations. Journal of Geotechnical and Geoenvironmental Engineering.

675   doi:10.1061/(ASCE)0733-9399(2004)130:10(1140).

676 Plassiard, J.-P., Belheine, N., and Donzé, F.-V. 2009. A spherical discrete element model: calibra-

677   tion procedure and incremental response. Granular Matter, **11**(5): 293–306.

678   doi:10.1007/s10035-009-0130-x.

679 Rorato, R., Arroyo, M., Andó, E., Gens, A., & Viggianni, G. (2020) Linking shape and rotation of

680   grains during triaxial compression of sand, under review, Granular Matter

681 Rorato, R., Arroyo, M., Andò, E., and Gens, A. 2019a. Sphericity measures of sand grains.

682   Engineering Geology, **254**(4): 43–53.

683 Rorato, R., 2019b. Imaging and discrete modelling of sand shape. PhD Thesis. Universitat

684   Politecnica de Catalunya (UPC).

685 Rorato, R., Arroyo, M., Gens, A., Andò, E., and Viggiani, G. 2018. Particle Shape Distribution

686   Effects on the Triaxial Response of Sands: A DEM Study. *In* micro to MACRO Mathematical

687   Modelling in Soil Mechanics, Trends in Mathematics. *Edited by* P. Giovine and et al. Reggio

688   Calabria (Italy). pp. 277–286. doi:10.1007/978-3-319-99474-1_28.

689 Rothenburg, L., & Bathurst, R. J. (1992). Micromechanical features of granular assemblies with

690   planar elliptical particles. Géotechnique, 42(1), 79-95.

691 Sakaguchi, H., Ozaki, E., and Igarashi, T. 1993. Plugging of the Flow of Granular Materials during

692   the Discharge from a Silo. International Journal of Modern Physics B, **7**(09–10): 1949–1963.

693   doi:https://doi.org/10.1142/S0217979293002705.

694 Shire, T., & O'Sullivan, C. (2013). Micromechanical assessment of an internal stability criterion.

695   Acta Geotechnica, 8(1), 81-90.

696 Skinner, A.E. 1969. A note on the influence of interparticle friction on the shearing strength of a

697   random assembly of spherical particles. Géotechnique, **19**(1): 150–157.

698   Vaid, Y., Chern, J., and Tumi, H. 1985. Confining pressure, Grain angularity and Liquefaction.

699   Journal of Geotechnical Engineering, **111**(10): 1229–1235.

700   Wadell, H. 1932. Volume, Shape, and Roundness of Rock Particles. The Journal of Geology, **40**(5):

701   443–451.

702   Wensrich, C.M., and Katterfeld, A. 2012. Rolling friction as a technique for modelling particle

703   shape in DEM. Powder Technology, **217**: 409–417. Elsevier B.V. doi:10.1016/j.pow-

704   tec.2011.10.057.

705   Wensrich, C.M., Katterfeld, A., and Sugo, D. 2014. Characterisation of the effects of particle shape

706   using a normalised contact eccentricity. Granular Matter, **16**(3): 327–337. doi:10.1007/s10035-

707   013-0465-1.

708   Williams, J. R., & Pentland, A. P. (1992). Superquadrics and modal dynamics for discrete elements

709   in interactive design. Engineering Computations, 9(2), 115-127.

710   Xiao, Y., Long, L., Matthew Evans, T., Zhou, H., Liu, H., and Stuedlein, A.W. 2019. Effect of

711   Particle Shape on Stress-Dilatancy Responses of Medium-Dense Sands. Journal of

712   Geotechnical and Geoenvironmental Engineering, **145**(2). doi:10.1061/(ASCE)GT.1943-

713   5606.0001994.

714   Yang, J., and Luo, X.D. 2015. Exploring the relationship between critical state and particle shape

715   for granular materials. Journal of the Mechanics and Physics of Solids, **84**: 196–213.

716   doi:10.1016/j.jmps.2015.08.001.

717   Zhang, N., Arroyo, M., Ciantia, M. O., Gens, A., & Butlanska, J. (2019). Standard penetration test-

718   ing in a virtual calibration chamber. Computers and Geotechnics, 111, 277-289.

719   Zhang, N., & Evans, T. M. (2019). Discrete numerical simulations of torpedo anchor installation

720   in granular soils. Computers and Geotechnics, 108, 40-52.

721   Zhao, D., Nezami, E. G., Hashash, Y. M., & Ghaboussi, J. (2006). Three-dimensional discrete ele-

722   ment simulation for granular materials. Engineering Computations, 23(7), 749-770.

723   Zhao, B., and Wang, J. 2016. 3D quantitative shape analysis on form, roundness, and compactness

724   with micro-CT. Powder Technology, **291**: 262–275. Elsevier B.V. doi:10.1016/j.pow-
725   tec.2015.12.029.

726   Zhao, S., Evans, T., & Zhou, X. (2018). Effects of curvature-related DEM contact model on the
727   macro-and micro-mechanical behaviours of granular soils. Géotechnique, 17(158), 21.

728   Zhou, B., Huang, R., Wang, H., and Wang, J. 2013. DEM investigation of particle anti-rotation
729   effects on the micromechanical response of granular materials. Granular Matter, **15**(3): 315–
730   326. doi:10.1007/s10035-013-0409-9.

731   Zhou, Y.C., Wright, B.D., Yang, R.Y., Xu, B.H., and Yu, A.B. 1999. Rolling friction in the dynamic
732   simulation of sandpile formation". Physica A: Statistical Mechanics and its Applications,
733   **269**: 536–553. doi:10.1016/j.physa.2005.01.019.

734